# Investigating Nanoparticle Organization in Polymer Matrices During Reaction-Induced Phase Transitions and Material Processing

Jacob A. LaNasa,<sup>a</sup> Anastasia Neuman,<sup>b</sup> Robert A. Riggleman,<sup>b</sup> Robert J. Hickey<sup>a,c,\*</sup>

<sup>a</sup>Department of Materials Science and Engineering, <sup>c</sup>Materials Research Institute, The Pennsylvania State University, University Park, Pennsylvania, 16801, United States

<sup>b</sup>Department of Chemical and Biomolecular Engineering, University of Pennsylvania, Philadelphia, PA, 19104, United States

#### **KEYWORDS**

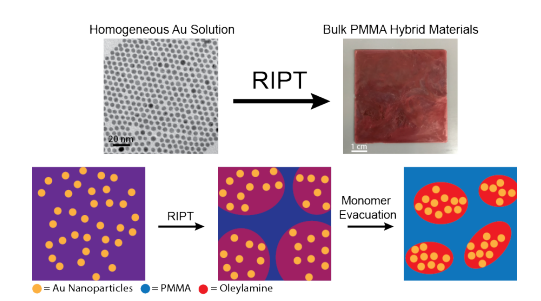
Polymer/inorganic nanoparticle hybrid materials, nanoparticle dispersion, in situ polymerization, thermodynamics of mixing, material processing

# **ABSTRACT**

Controlling nanoparticle organization in polymer matrices has been and is still a long-standing issue, and directly impacts the performance of the materials. In the majority of instances, simply mixing nanoparticles and polymers leads to macroscale aggregation, resulting in deleterious effects. An alternative method to physically blending independent components such as nanoparticle and polymers is to conduct polymerizations in one-phase monomer/nanoparticle mixtures. Here, we report on the mechanism of nanoparticle aggregation in hybrid materials in which gold nanoparticles are initially homogeneously dispersed in a monomer mixture, and then undergo a two-step aggregation process during polymerization and material processing. Specifically, oleylamine-functionalized gold nanoparticles (AuNP) are first synthesized in a methyl methacrylate (MMA) solution, and then subsequently polymerized using a free radical polymerization initiated with azobisisobutyronitrile (AIBN) to create hybrid AuNP and poly(methyl methacrylate) (PMMA) materials. The resulting products are easily pressed to obtain

bulk films with nanoparticle organization defined as either well-dispersed or aggregated. Polymerizations are performed at various temperatures (T) and MMA volume fractions ( $\Phi_{\text{MMA}}$ ) to systematically influence the final nanoparticle dispersion state. During the polymerization of MMA and subsequent material processing, the initially homogeneously AuNP/MMA mixture undergoes macrophase separation between PMMA and oleylamine during the polymerization, yet the AuNP are dispersed in the oleylamine phase. The nanoparticles then aggregate within the oleylamine phase when the materials are processed via vacuum drying and pressing. Nanoparticle organization is tracked throughout the polymerization and processing steps using a combination of transmission electron microscopy (TEM) and small-angle X-ray scattering (SAXS). The resulting dispersion state of AuNPs in PMMA bulk films is ultimately dictated by the thermodynamics of mixing between the PMMA and oleylamine phases, but the mechanism of nanoparticle aggregation occurs in two steps that correspond to the polymerization and processing of the materials. Flory Huggins mixing theory is used to support the PMMA and oleylamine phase separation. The reported results highlight how the integration of non-equilibrium processing and mean-field approximations reveal nanoparticle aggregation in hybrid materials synthesized using reaction-induced phase transitions.

## For Table of Contents Only



## **INTRODUCTION**

Hybrid materials created by mixing polymer and inorganic nanoparticles have been a focused area of research within the materials community over the last 30 years.<sup>1–4</sup> The primary motivation for creating new hybrid materials is to improve existing material properties in polymer systems, or introduce new functionality to polymers using inorganic fillers (*i.e.*, metals and oxides).<sup>5–15</sup> Regardless of the desired material property, mixing polymer and inorganic nanoparticle components is a challenging thermodynamics problem, as unfavorable interactions quantified by the Flory-Huggins interaction parameter ( $\chi$ ) and large degrees of polymerization in polymer phases (N) create significant barriers to mixing.<sup>4,16</sup>

Strategic blending of polymers and inorganic nanoparticles include "softening" the penalties of mixing. Specifically, treatment of the particle surfaces with ligands, small molecules, or polymers will reduce the enthalpic penalties of mixing within the polymer phase.  $^{17-20}$  Furthermore, high functional group density  $(\sigma)$ , and ratio between the degrees of polymerization of the grafted polymer chain (N) and the matrix (P)  $(e.g., N/P = \alpha \ge 0.2)$  prevents nanoparticle/polymer dewetting.  $^{16,21}$  The compatibilization of polymer-functionalized nanoparticles within homopolymer, binary, and ternary blends, both within bulk phases and at film interfaces, is an active area of research.  $^{22-26}$  While these strategies have been effective, surface modification methods tend to be extensive, and the solution blending and annealing processes make the materials challenging to scale. Often times, surface-initiated polymerization on a functional particle surface is required to achieve sufficiently high group density at large enough molecular weights to have entropically favorable surface/matrix interactions.  $^{19,27-31}$ 

Alternative methods include kinetically "trapping" particle components in polymer matrices to limit phase separation.<sup>32–34</sup> In this instance, non-equilibrium processes are effective at rapidly changing the state of a system (*e.g.*, glass transition, crystallization, *in situ* polymerizations) with the goal that solubilized particles lack sufficient mobility to relax to a thermodynamically

favorable state. 18,35–37 The drawback to these methods, given that the low solubility criterion remains, is that the particle morphologies are metastable, and will continue to phase separate over time given sufficient freedom. An example is heating the material above the glass transition temperature during processing, which will enable nanoparticle diffusion. 38–41

One of the most straightforward ways to facilitate a phase change within a system is through a chemical reaction. 42-44 Under specific conditions, chemical reactions proceed rapidly and with triggers such as temperature, 45 light, 46 and mechanical activation. 47 An example of a reaction-induced phase transition (RIPT) is frontal polymerization. 48 During a frontal polymerization, the thermal initiation and heat transport from a highly exothermic polymerization reaction drives the propagation of a polymerization front. With unstable front propagation, the polymerization process will spontaneously generate thermal instabilities, leading to complex microstructures in polymer materials. 45,48

There are numerous advantages to using RIPT for dispersing nanoparticles within a polymer matrix. Nanoparticles with functionalized surfaces are easily solubilized within a solution phase, even if there are non-negligible enthalpic interactions, affording homogeneous dispersion without interference from entropic mixing barriers associated with reduced  $\alpha$  values. As a nanoparticle/monomer mixture polymerizes, the polymer matrix degree of polymerization increases, driving up the segregation strength ( $\chi N$ ) of the mixture, favoring phase separation. Note, Flory-Huggins theory assumes that  $\chi$  is constant between two components when one component is either the monomer or the polymer. If the vitrification of the system due to increases in the glass transition temperature ( $T_g$ ) or crosslinking occurs before the two components macroscopically phase separate, the resulting materials will have well-dispersed nanoscale objects in the polymer matrix. Recent work has similarly shown that carbon nanoparticles, graphite, and polymer-functionalized nanoparticles can be dispersed within a polymer matrix through similar methods. 45,49,50 Although there are examples of "trapping" nanoscale objects within polymer

matrices during *in situ* polymerizations, there is a need to establish a foundational framework that incorporates N and  $\chi$  to predict changes in the phase behavior during the progression of the polymerization from a thermodynamic perspective that also accounts for the kinetics of the reaction to control nanoparticle dispersion in hybrid polymer materials.

To investigate RIPT as a strategy to control nanoparticle dispersion in polymer matrices, we systematically studied the phase separation and resulting particle dispersion after polymerization and material processing. Specifically, a ternary solution blend of methyl methacrylate (MMA), oleylamine, and oleylamine-functionalized gold nanoparticles are polymerized using a free radical polymerization initiated with azobisisobutyronitrile (AIBN) and are vacuum pressed to obtain bulk materials (Figure 1). Within the process, a new procedure for synthesizing and stabilizing oleylamine-functionalized gold nanoparticles (AuNP) within a monomer phase is reported. Polymerizations are performed at various temperatures (T) and MMA volume fractions ( $\Phi_{\text{MMA}}$ ) to systematically influence the final nanoparticle dispersion state. Nanoparticle dispersion is established using a combination of transmission electron microscopy (TEM) and small-angle Xray scattering (SAXS). The resulting AuNP dispersion in poly(methyl methacrylate) (PMMA) bulk films are understood in the context of Flory Huggins mixing theory. During the polymerization of MMA and material processing procedures, the initially homogeneously mixed AuNP/MMA mixture undergoes phase separation in which PMMA and oleylamine form two separate phases, while the nanoparticles reside in the oleylamine phase. The reported results highlight how the integration of non-equilibrium processing and mean-field approximations reveal nanoparticle aggregation in hybrid materials synthesized using reaction-induced phase transitions.

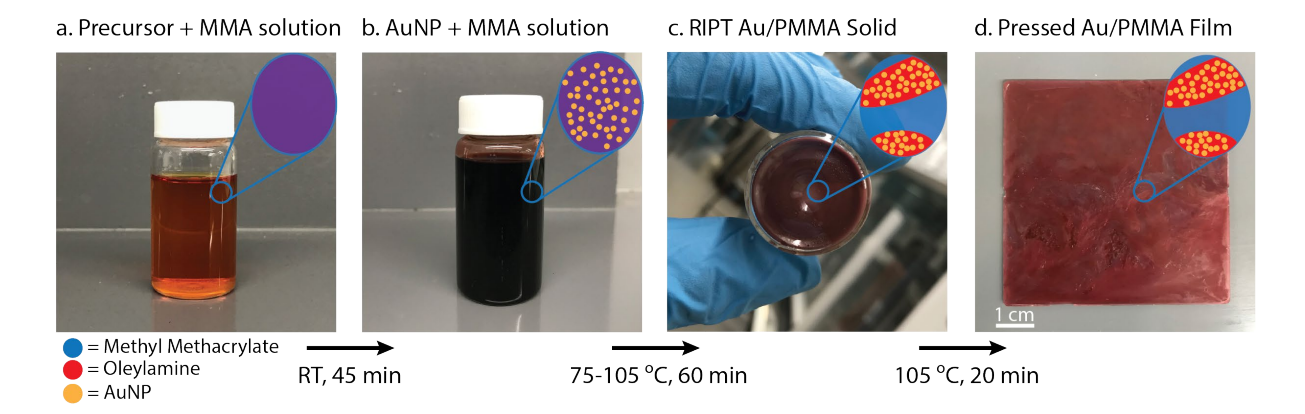


**Figure 1.** Synthesis and processing of AuNP/PMMA hybrid materials. **a)** AuNP precursors (Gold(III)chloride trihydrate, oleylamine) are added to purified MMA monomer before **b)** the reducing agent (borane *tert*-butylamine complex) initiates AuNP synthesis at room temperature. **c)** Particles are then diluted to a known volume fraction with additional MMA and a radical initiator (AIBN) before polymerization is initiated, quenched after 60 min, and dried under vacuum. **d)** Samples are then vacuum pressed into bulk samples for characterization.

## **EXPERIMENTAL SECTION**

## **Materials**

Gold (III) chloride trihydrate, oleylamine (70%), borane *tert*-butylamine complex, methyl methacrylate (MMA), and azobisisobutyronitrile (AIBN) were purchased from Sigma Aldrich and used as received. Tetrahydrofuran was purchased from ThermoFisher Scientific and used as received. Alumina was purchased from Honeywell.

# Poly(methyl methacrylate)/Gold Nanoparticle Hybrid Material Synthesis

AuNPs were prepared using a modified procedure.<sup>51</sup> Gold (III) chloride trihydrate (100 mg), MMA (8 mL) and oleylamine (8 mL) were added to a 20 mL scintillation vial and stirred under ambient conditions. In a second vial, borane *tert*-butylamine complex (50 mg) was dissolved in oleylamine (1 mL) and methyl methacrylate (1 mL). The borane *tert*-butylamine solution was then added into

the precursor solution under magnetic stirring and left to react for 45 min. AuNP/MMA solutions (3 mL) were mixed with AIBN (1.0 wt% with respect to MMA) and sonicated (10 s) before sealing and placing in a vacuum oven for 60 min. After polymerization, sample vials were frozen in liquid nitrogen and dried under vacuum overnight (< 50 mTorr) to remove unreacted monomer.

## **Bulk Film Processing**

Samples were removed from their glass vials and placed in a pressing mold between two Kapton films. Samples were pressed under vacuum at 105 °C for 20 min.

## **Material Characterization**

UV-vis-NIR spectroscopy (UV-Vis)

UV-vis spectra were measured using an Agilent Cary 60 UV-vis spectrometer for bulk films and solutions contained within a quartz cuvette. Scanning wavelength ranges were from 200 nm to 800 nm. Air and a pressed pure PMMA film were used as the blank to correct for baseline. Prior to solution measurement, particles solutions were washed by precipitation in ethanol, centrifugation, and redispersion in fresh MMA. Bulk film spectra were measured as prepared and were normalized by the local maximum of the absorption peak.

# Transmission electron microscopy (TEM)

Micrographs are taken with a FEI Tecnai G2 Spirit BioTwin TEM. AuNPs in solution were prepared by precipitating the particle solution with ethanol, centrifuging (10,000 rpm, 5 min), and redispersing in fresh MMA prior to drop casting onto TEM grids (Electron Microscopy Sciences, formvar/carbon 200 mesh, copper). Drop casting as-prepared samples gave poor images due to the excess oleylamine. Sections of polymerized and pressed samples were microtomed into 70-90 nm sections using a Leica UC6 ultramicrotome and were kept under vacuum overnight prior to imaging. Particle sizes were determined using ImageJ.

## Small-angle X-ray scattering (SAXS)

Transmission SAXS measurements are performed using a Cu K- $\alpha$  sourced (1.54 Å and 8.04 keV) Xeuss 2.0 (XENOCS) instrument installed with collimation optics and a 2D X-ray detector Pilatus 200K (Dectris). The sample to detector distances were calibrated using a silver behenate powder standard. Samples were exposed for 5 min and their 2D isotropic scattering intensities were azimuthally integrated to obtain I(q) vs. q plots. Particle solution samples were measured in quartz capillaries (1.5 mm, Charles Supper Company) and PMMA films were measured using a bulk stage.

# Spinodal Calculation

The boundary of the spinodal regime can be plotted as a function of  $N_{\rm OAm}$ ,  $N_{\rm PMMA}$ , and  $\Phi_{\rm MMA}$ .

$$\chi_{Spin}(N_{PMMA}, N_{OAm}, \Phi_{MMA}) = \frac{1}{2} \left( \frac{1}{N_{PMMA} \Phi_{MMA}} + \frac{1}{N_{OAm} (1 - \Phi_{MMA})} \right)$$

## Binodal Calculation

The binodal curve for the system is calculated analytically by finding the common tangents of the Gibbs free energy of mixing with respect to composition,

$$\frac{\Delta G_m}{k_B T} = \frac{\Phi_{MMA}}{N_{PMMA}} Ln(\Phi_{MMA}) + \frac{1 - \Phi_{MMA}}{N_{OAm}} Ln(1 - \Phi_{MMA}) + \chi_{eff}(\Phi_{MMA})(1 - \Phi_{MMA})$$

where the condition for the binodal composition is defined as

$$\frac{\partial \Delta G_m}{\partial \Phi_{MMA}^{(1)}} = \frac{\partial \Delta G_m}{\partial \Phi_{MMA}^{(2)}}.$$

To find the common tangents, a double Legendre-Fenchel transform was performed on the Gibbs free energy, where the transform is defined as

$$f^{*}(k) = \sup_{x} \{kx - f(x)\}$$
$$f^{**}(x) = \sup_{k} \{kx - f^{*}(k)\}.$$

The function  $f^{**}(x)$  is the convex envelope of the original function f(x). The points at which  $f^{**}(x)$ , the double Legendre-Fenchel transform of the Gibbs free energy, intersects with f(x), the Gibbs free energy itself, represent the common tangents of f(x). For each value of  $\chi$ , these intersection points give the binodal composition for the system.

## RESULTS AND DISCUSSION

Gold nanoparticles (AuNPs) were synthesized using an adapted particle preparation method in which methyl methacrylate (MMA) monomer was used as the solvent.<sup>51</sup> The gold precursor (gold(III)chloride trihydrate) was reduced at room temperature upon addition of borane *tert*-butylamine, and the AuNPs were sterically stabilized within solution due to surface adhesion of oleylamine (OAm). The synthesis of AuNP within the MMA phase streamlined blend preparation into a single-pot process where AIBN (1.0 wt% with respect to total MMA) and additional MMA monomer are added to the particle solution prior to polymerization without need for additional purification. Size and optical properties of AuNPs prepared under this procedure were characterized using UV-Vis, TEM, and SAXS and the results are shown in **Figure 2**.

The AuNPs possess a maximum absorption peak at  $\lambda_{\text{max}} = 512$  nm, which is similar to the absorbance of OAm-modified AuNPs in the same size range.<sup>51,53</sup> The particle diameter (d = 5.5 nm) was determined *via* size analysis of TEM micrographs (**Figure S1**) and verified through fitting the 1D SAXS profile to a spherical form factor. The nanoparticle size is predicted to provide fast diffusion kinetics, as the Stokes-Einstein diffusion coefficient scales as  $D_0 \approx d^{-1}$ . The

characteristically fast diffusion rate due to particle size allows for unambiguous identification of particle dispersion.<sup>49</sup>

AuNP/MMA blends were prepared by diluting the initial MMA volume fraction ( $\Phi_{\text{MMA}} = 50\%$ ) into four solution concentrations, with  $\Phi_{\text{MMA}}$  equal to 90, 85, 80, and 75%. By mass, these samples corresponded to AuNP concentrations between 0.5-2 mg/mL respectively and by volume represented a small fraction ( $\Phi_{\text{NP}} \approx 10^{-5}$ ) of the remaining volume occupied by the oleylamine and AuNP components. Blends that were polymerized under the initial particle synthesis conditions ( $\Phi_{\text{MMA}} = 50\%$ ) yielded co-existing solid and liquid phase-separated mixtures (**Figure S2**). Alternatively, the dilution of the initial AuNP solutions with MMA lead to free-standing and homogeneous material after conducting polymerizations for 60 min, quenching in liquid nitrogen, drying under vacuum overnight (< 50 mTorr), and vacuum pressing into bulk films (**Figure 1**).

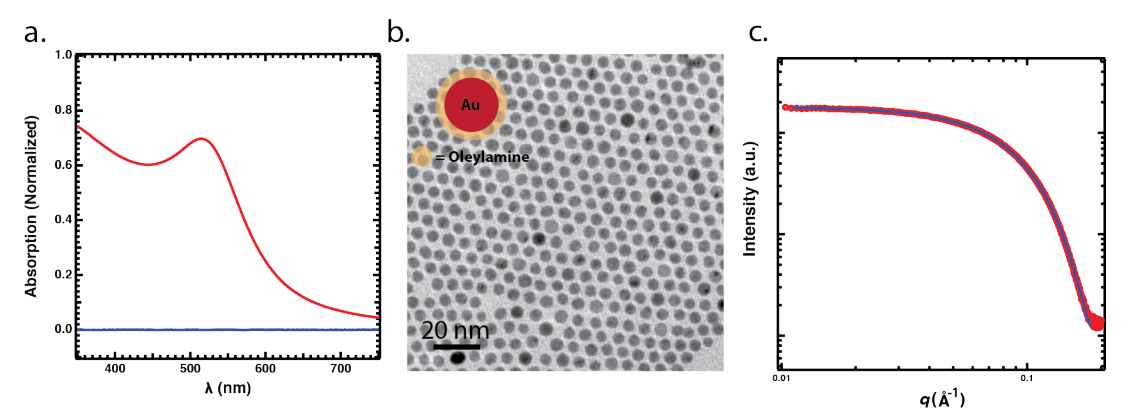


Figure 2. Characterization of AuNPs synthesized in MMA. a) UV-Vis absorption spectra of AuNPs (red) in a methyl methacrylate monomer solution with a max absorption peak  $\lambda_{\text{max}} = 512$  nm. The blue trace is of the pure MMA liquid. b) Electron micrograph of AuNPs ( $d = 5.5 \pm 0.4$  nm). c) SAXS profile (red) of AuNPs in reaction solution and fit to a spherical form factor (blue) with particle diameter  $d = 4.9 \pm 0.2$  nm.

Aliquots (3 mL) of AuNP/MMA solutions ( $\Phi_{\text{MMA}} = 90, 85, 80, \text{ and } 75\%$ ) were mixed with the radical initiator AIBN (1 wt% with respect to MMA) and were thermally initiated to polymerize the solutions at three respective temperatures (T = 75 °C, 90 °C, and 105 °C) for 60 min. AIBN was used to thermally initiate the polymerization of the MMA phase, and was chosen over other radical initiators (i.e., benzoyl peroxide) due to its reportedly low decomposition temperature and temperature-variable polymerization rate.<sup>54</sup> All samples, to some degree autoaccelerate during the polymerization, but samples polymerized at 105 °C boil and increase in solution viscous within 5-15 min of being placed within the oven. Reacted samples were quenched in liquid nitrogen and dried under vacuum overnight (< 50 mTorr) to remove any unreacted monomer prior to bulk film pressing. Sample conversions were obtained for each condition and the results are reported in **Table S1.** Conversions ranged from 64-92% with a general trend of 75 °C having the highest yields and 105 °C having the lowest yields, which is partially attributed to monomer evaporation during polymerization. Sample conversion was also lower than that of a 100% PMMA control polymerized under identical conditions ( $\Phi_{\text{MMA}} = 100\%$ ). Whether the conversion difference is due to the presence of non-polymerizing ligands or an inhibited polymerization will be a topic of future discussion. Materials evacuated of unreacted monomer were then pressed into bulk films at 105 °C for 20 min with a representative photograph of  $\Phi_{\text{MMA}} = 90\%$ , T = 75 °C presented in **Figure 1**. Films were pressed under these conditions to minimize the influence of pressing on nanoparticle aggregation. Furthermore, it is possible to press these samples at 105 °C due to the plasticization of the materials containing oleylamine and PMMA oligomers, similar to previously reported work.49,50

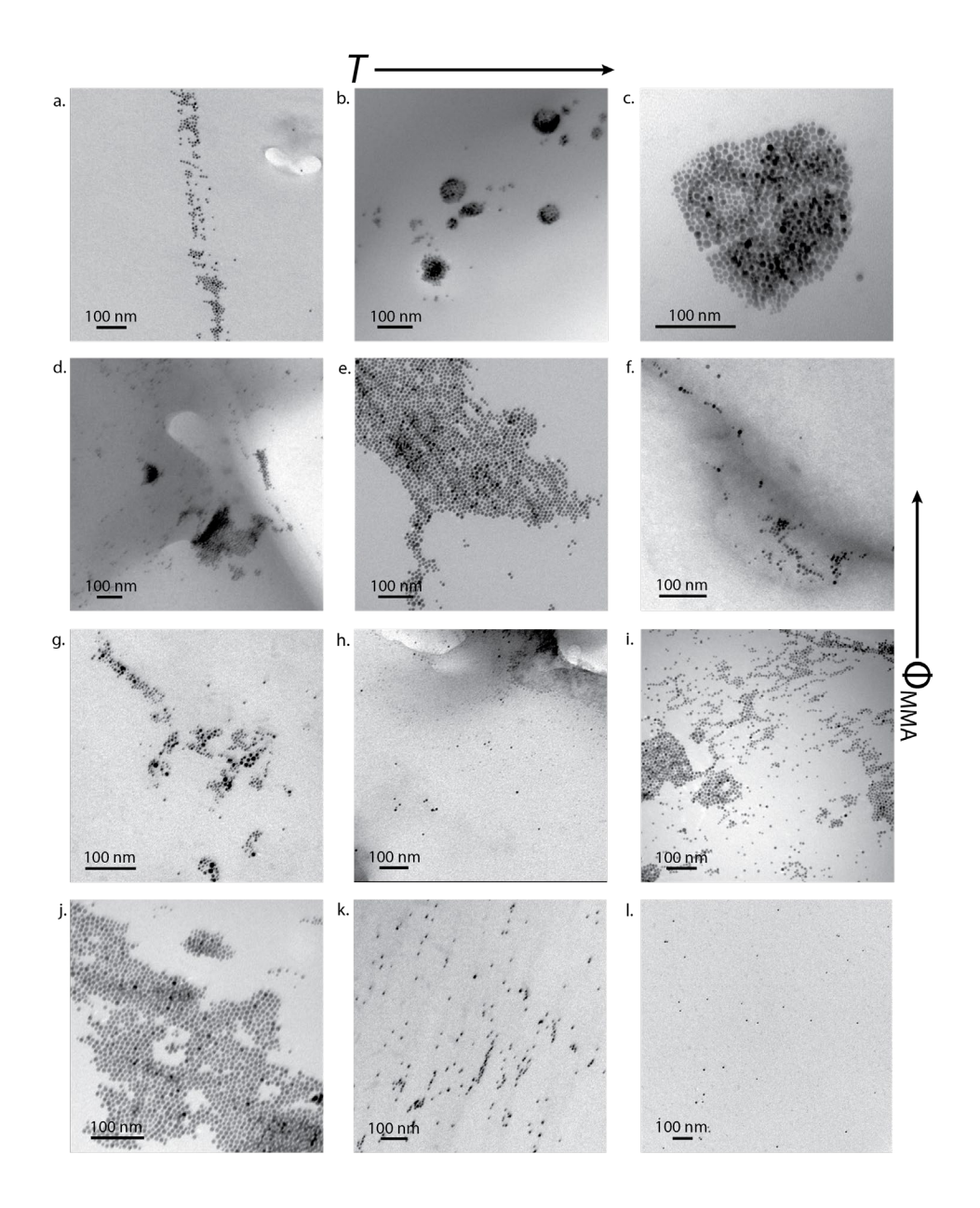


Figure 3. Representative micrographs of the AuNP dispersion within PMMA under different reaction conditions. Samples were obtained by microtoming sections of bulk films three weeks after pressing. Blends were polymerized with  $\Phi_{\text{MMA}}$  volume fractions of **a-c**) 90%, **d-f**) 85%, **g-i**) 80%, and **j-l**) 75% with the left most column of images corresponding to reaction temperatures of 75 °C, the center column of images corresponding to reaction temperatures of 90 °C, and the right most column of images corresponding to reaction temperatures of 105 °C, respectively.

After pressing, bulk samples were microtomed and AuNP dispersion states were inspected using TEM. Representative micrographs of AuNPs within polymer matrices are presented in Figure 3. Under all reaction conditions, AuNPs were found to have preserved their initial spherical shape and steric stabilization when aggregated. The stability of the nanoparticles is attributed to the oleylamine surface-functionality being preserved during the course of the reaction, sample drying, and sample processing. The absence of AuNP agglomeration and coalescence was macroscopically quantifiable as well, as the optical properties within the bulk film were not found to change significantly across samples (Figure S3). Despite the interparticle stability, particle sizes were found to increase from their initial size (d = 5.5 nm, as measured using TEM) to diameters ranging from  $\approx$  6-10 nm over the course of polymerization and pressing. A summarizing table of size increase is presented in Table S2. AuNP size increase and coalescence was initially expected due to the thermal nature of the reaction, but the minimal size increase and notable particle stabilization in the materials was an unexpected result. Typically, in situ polymerizations (thermal or otherwise) with gold nanoparticles are expected to favor agglomeration and particle coalescence, so the preservation on individual nanoparticle shape and absorption properties are notable advantages to utilizing an oleylamine-functionalized AuNP surface. 46,53

Within the micrographs presented in **Figure 3**, there are varied degrees of particle aggregation. For convention, the authors refer to observed nanoparticle dispersion states after polymerization and bulk film processing as either well-dispersed or aggregated. Interestingly, some aggregated regions of micrographs displayed dispersion states resembling particle strings, clusters, and nanosheets that are seen and resemble previously reported equilibrium dispersion states in

polymer-functionalized nanoparticle/homopolymer systems.<sup>21</sup> Although here the nanoparticle dispersion states are defined as either well-dispersed or aggregated, the degree of aggregation in samples is not easily quantified using real space imaging. As evidenced above, a degree of coexistence between aggregation and particle dispersion is seen in several of the images shown in **Figure 3**, which makes identification of the bulk dispersion state ambiguous. Additionally, air and material interfaces resulting from the auto accelerating reaction are easy to see in microscopy but are not expected to significantly contribute to the bulk dispersion state. As a result, identification of the influence of reaction conditions, namely temperature and  $\Phi_{\text{MMA}}$  on AuNP dispersion state are quantified using other means.

Specifically, SAXS was used to quantify the degree of aggregation within the processed bulk materials of samples polymerized under three temperatures (75 °C, 90 °C, and 105 °C) and four volume fractions ( $\Phi_{\text{MMA}} = 90$ , 85, 80, and 75%). Here, the reciprocal space information allows for an ensemble measurement of particle-particle correlations that are apparent when particles aggregate at the relevant length scale. The resulting 1D profiles of SAXS measurements are included in **Figure 4.** Primary scattering peaks ( $q^* = 2\pi/d^*$ ) corresponding to the center-to-center distance of the particles were evident in all samples except for  $\Phi_{\text{MMA}} = 75\%$  at 90 °C and 105 °C, and  $\Phi_{\text{MMA}} = 80\%$  at 90 °C (**Table S3**). The  $q^*$  shows no discernable trend at constant  $\Phi_{\text{MMA}}$  across T, but show constant correlation at T = 75 °C, and decreased correlations at T = 90 °C and 105 °C with decreasing  $\Phi_{\text{MMA}}$ . Combined with real space imaging of **Figure 3**, the measured  $q^*$  is attributed to strong correlations between closely packed particles at T = 75 °C and weaker correlations with more diffuse particle spacings at T = 90 °C and 105 °C.

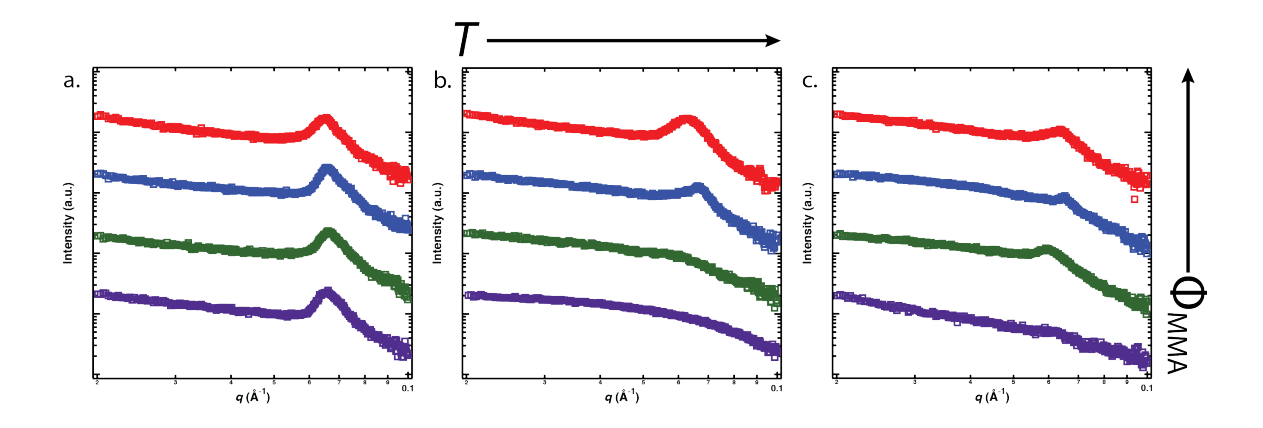


**Figure 4.** 1D SAXS profiles of Au/PMMA bulk films displaying interparticle correlations. Processing conditions  $(T, \Phi_{\text{MMA}})$  correspond to **a**) T = 75 °C **b**) T = 90 °C **c**) T = 105 °C and  $\Phi_{\text{MMA}} = 90\%$  (red),  $\Phi_{\text{MMA}} = 85\%$  (blue),  $\Phi_{\text{MMA}} = 80\%$  (green), and  $\Phi_{\text{MMA}} = 75\%$  (purple) respectively.

The extent of nanoparticle aggregation presented in **Figures 3** and **4** is hypothesized to be due to competing thermodynamic driving force for macrophase separation between PMMA and OAm in which AuNPs reside in the OAm phase, and material processing procedures. Considering that multiple reaction and processing steps are undertaken to arrive at the final bulk hybrid material, it is necessary to identify multiple contributing factors that influence nanoparticle dispersion. Here, we discuss the thermodynamically expected equilibrium state of the mixture and influence of thermal processing on AuNP reorganization.

For  $\Phi_{\rm MMA}$  = 75% reaction conditions conducted at three different temperatures shown in **Figure 4** (purple curves), a transition from aggregation to well-dispersed particles is apparent as the reaction temperature increases from 75 °C to 105 °C. To investigate the transition, quartz capillaries were filled with the  $\Phi_{\rm MMA}$  = 75% solution mixture and scattering profiles were compared before and

after polymerization at each of the three respective temperatures (**Figure 5**). It is apparent in **Figure 5** that no correlation peak indicating nanoparticle aggregation forms within the region of interest ( $q \approx 0.06$ -0.07 Å<sup>-1</sup> per **Figure 4**). The absence of the correlation peak indicates, despite the aggregation seen within the bulk materials, that AuNPs stay well-dispersed during the 60 min polymerization. Interestingly, the shift in scattering curves to lower q at increased temperatures indicate that the particle size changes during the polymerization which is consistent with the TEM images. The SAXS results shown in **Figure 5** suggest that AuNP aggregation shown in **Figures 3** and **4** are not triggered by the polymerization, but are predicted to occur during the processing of the bulk materials.

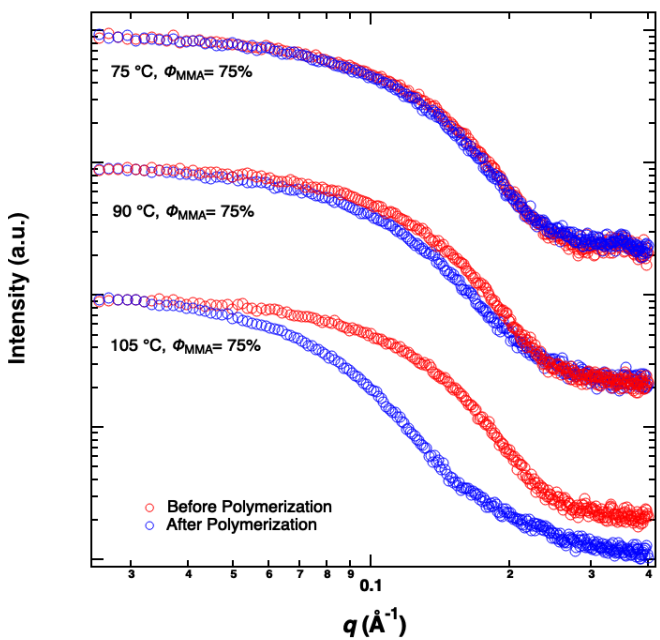
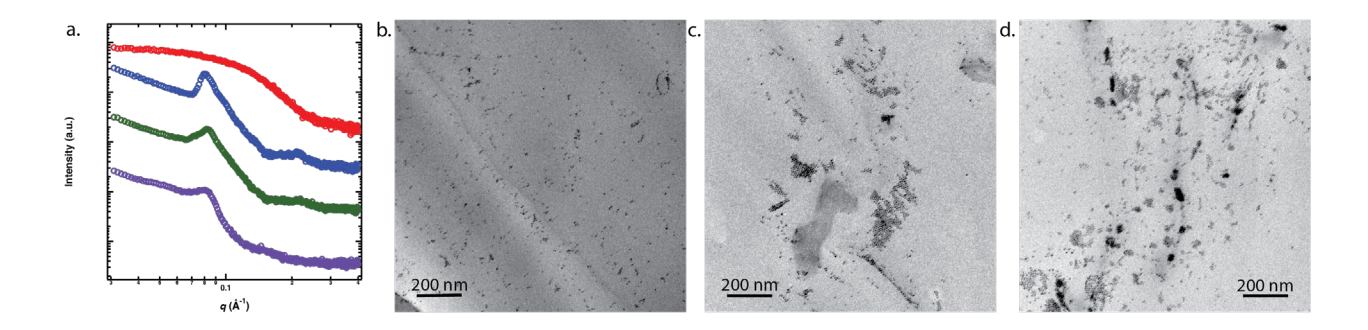


Figure 5. 1D SAXS profiles of  $\Phi_{\text{MMA}} = 75\%$  solutions prior to polymerization (red circles) and post polymerization (blue circles) at each reaction temperature (75, 90, 105 °C, respectively).

To confirm that the nanoparticle aggregation occurs during the material processing, SAXS patterns and TEM images were acquired for the sample  $\Phi_{\text{MMA}} = 75\%$  at T = 75 °C, which is the reaction

condition known to exhibit nanoparticle aggregation in the final state (**Figures 3** and **4**) but remain well dispersed after polymerization (**Figure 5**). The material formed under the specified condition was measured at three distinct processing stages: after vacuum drying, after 20 min of pressing under vacuum at 105 °C, and after five days of annealing at 105 °C. The additional imaging of the processed sample thermally annealed at 105 °C for five days was performed to provide particles sufficient mobility to reach their equilibrium phase separated state. The results of the processing study are presented in **Figure 6**.



**Figure 6.** The influence of drying, pressing, and annealing on AuNP dispersion for hybrid samples synthesized at T = 75 °C and  $\Phi_{\text{MMA}} = 75\%$ . **a)** 1D SAXS profiles showing a transition in dispersion from well-dispersed in the polymerized blend (red curve) to aggregated upon vacuum drying (blue). The dispersion state is maintained upon material pressing (green) and thermal annealing at 105 °C for five days (purple). Micrographs of microtomed samples for **b)** the vacuum dried sample, **c)** the pressed sample, and **d)** anneal sample show representative AuNP dispersion within the material.

By comparing the SAXS profiles of the polymerized blend (red) to the vacuum dried sample (blue) in **Figure 6a**, it is apparent that the particle correlation peak associated with aggregation forms

upon vacuum drying. The vacuum drying step is done to evacuate unreacted MMA monomer within the vitrified melt after polymerization. Therefore, it is expected that on removal of unreacted MMA,  $\Phi_{\text{MMA}}$  reduces, promoting nanoparticle aggregation. The formation of the correlation peak in the SAXS pattern shown in **Figure 6** upon vacuum drying persists when the material is pressed, and stays at a constant  $q^*$  during the five days of thermal annealing at the processing temperature (105 °C). Furthermore, the scattering profile does not significantly change within the 20-min processing time scale, suggesting that AuNP reorganization is minimal during the process. Additionally, the correlation peak is maintained after, indicating that particle reorganization occurs primarily during the drying process. Micrographs of each of these three conditions show dispersion states consistent with the scattering profiles, with sterically stabilized AuNPs dispersed throughout the matrix in varied degrees of aggregate assemblies.

While it is expected that the removal of unreacted MMA after the polymerization would reduce the distance between particles, the apparent nanoparticle transition from well-dispersed after polymerization to aggregated structures when processed is unexpected. To understand the nanoparticle dispersion state transition, it is useful to consider the binary phase behavior of OAm and PMMA and interpret particle dispersion through the resulting context. Over the course of the presented work, initial OAm and MMA monomer blends were miscible within the specified temperature and composition ranges (T = 25-105 °C,  $\Phi_{\text{MMA}} = 75-90\%$ ). A representative AuNP-free  $\Phi_{\text{MMA}} = 75\%$  sample before polymerization is shown in **Figure 7a**. However, upon polymerization at the three reported temperatures (T = 75 °C, 90 °C, and 105 °C), OAm/PMMA mixtures are visibly seen to phase separate, as shown in the photographs presented in **Figure 7b-d**. Since the AuNP volume fraction ( $\Phi_{\text{NP}} \approx 10^{-5}$ ) is assumed to minimally interfere with the

polymerization under these conditions, we assume that the phase transition occurs in AuNP solutions as well, with the OAm-functionalized AuNPs undergoing a similar phase transition to the OAm-rich minority phase. As unreacted MMA monomer is both miscible with PMMA and OAm phases, we hypothesize that the removal of MMA from the polymerized blend reduces the volume of the OAm-rich minority phases where the initially well-dispersed AuNPs have migrated and drives the observance of the nanoparticle aggregation shown in the SAXS patterns of **Figure 6a**. An interesting implication of this hypothesis is that, while AuNPs are macroscopically phase separated into OAm-rich phases, they can be considered well-dispersed at the nm length scale in the OAm-rich prior to MMA removal, as confirmed in the SAXS pattern of **Figure 5**.

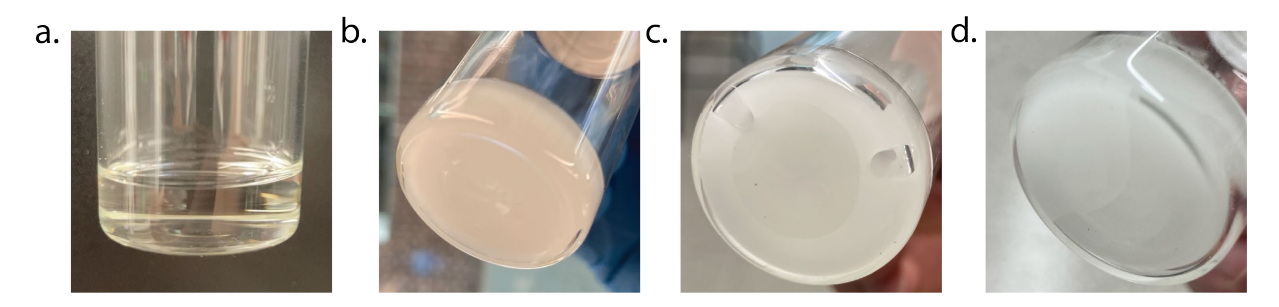


**Figure 7.** Visible observation of a one-to-two-phase transitions upon polymerization of OAm/MMA blends. **a)** an AuNP-free  $\Phi_{\text{MMA}} = 75\%$  mixture is initially transparent and homogeneous prior to polymerization. After polymerization at **b)**  $T = 75 \, ^{\circ}\text{C}$ , **c)**  $T = 90 \, ^{\circ}\text{C}$ , and **d)**  $T = 105 \, ^{\circ}\text{C}$ , samples are visibly cloudy, signifying macrophase separation.

The results above are supported by calculating the predicted equilibrium binary phase diagram of OAm/PMMA blends. To consider the equilibrium state of the blend, we approximate the blend as a binary mixture of MMA and OAm, with MMA undergoing a chemical reaction (*N*<sub>PMMA</sub> increasing from 1 to an achievable upper limit during polymerization). Flory-Huggins mixing

theory is useful for determination of predicted thermodynamic state of these systems. Due to the low overall volume fraction of nanoparticles (**Table S4**), the AuNP contribution to the free energy of mixing is assumed to be minimal, despite their non-negligible impact to the resulting optical properties (**Figure S3**). In the case of mixing MMA and OAm phases, the Gibbs free energy of mixing for the initial state before polymerization is given as,

$$\frac{\Delta G_m}{k_B T} = \frac{\Phi_{MMA}}{N_{PMMA}} \ln(\Phi_{MMA}) + \frac{1 - \Phi_{MMA}}{N_{OAm}} \ln(1 - \Phi_{MMA}) + \chi_{eff}(\Phi_{MMA}) (1 - \Phi_{MMA})$$
 Eq. 1

Where  $N_{\text{PMMA}}$  is the degree of polymerization of the MMA phase and  $\chi_{eff}(T) \approx \frac{V_{MMA}(\delta_{MMA} - \delta_{OAm})^2}{N_A k_B T} + 0.34$  is the effective interaction parameter between MMA and OAm calculated using values for the solubility parameters  $\delta_{MMA} = 18.8 \text{ MPa}^{1/2}$  and  $\delta_{OAm} = 16.6 \text{ MPa}^{1/2}$  reported in the literature. S2,55 Here,  $\chi_{eff}$  is a pairwise interaction and is expected to stay constant during the polymerization even though MMA is converted to PMMA. There is a possibility that  $\chi_{eff}$  changes as MMA is consumed to form PMMA, but for now, it is assumed that  $\chi_{eff}$  is constant during the polymerization. The Flory-Huggins lattice site volume can be defined as the volume of an MMA monomer, and we approximate the  $N_{\text{PMMA}}$  as the maximal conversion that was determined experimentally (**Table S1**) using size-exclusion chromatography (**Table S5**,  $\Phi_{\text{MMA}} = 100\%$ ,  $N_{\text{PMMA}} = 1030$ ), and the volumetric degree of polymerization of OAm,  $N_{\text{OAm}} \approx V_{\text{OAm}}/V_{\text{MMA}} \approx 4$ . From this, a predicted phase diagram can be calculated and is presented in **Figure 8**.

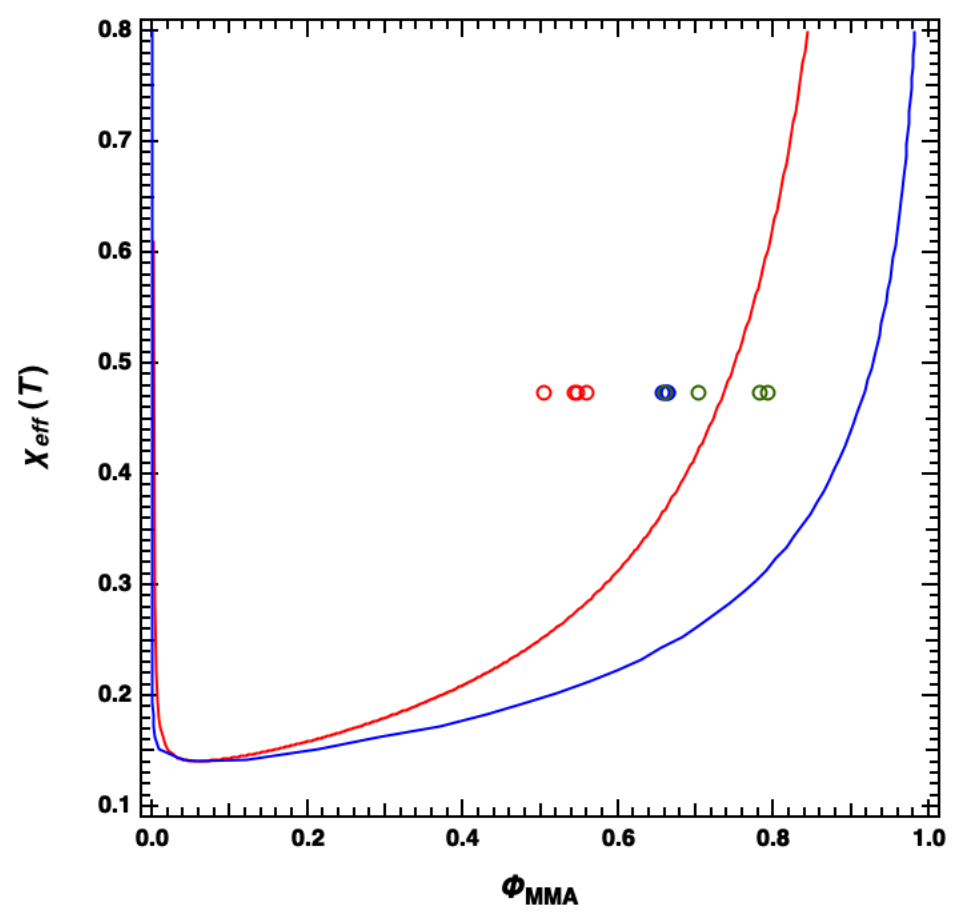


**Figure 8.** Predicted phase diagram of a PMMA/OAm blend after vacuum drying. The binodal (blue curve) and spinodal regions (red) are calculated based on the lattice site volume being the molar volume of MMA, with  $N_{\text{MMA}} = 1030$ ,  $N_{\text{OAm}} = 4$ . The corresponding  $\Phi_{\text{MMA}}$  (corrected using reaction conversions), the  $\chi_{eff}(T)$  of the processing step (105 °C,  $\chi_{eff} = 0.474$ ), and the reaction temperatures (T = 75 °C, green; 90 °C, blue; and 105 °C, red) are represented by the open circles.

As AuNP aggregation is hypothesized to occur during the vacuum drying phase, the  $\Phi_{\text{MMA}}$  values for each sample are adjusted using the reaction conversions reported in **Table S1**, with the assumption that all mass loss during drying is from unreacted MMA. Using the data from **Table S1**, and the approximate  $\chi_{\text{eff}}$  of the processing temperature (105 °C,  $\chi_{\text{eff}} = 0.474$ ), each reaction

condition is predicted to lie within the two-phase region of the OAm and PMMA phase diagram when at equilibrium. As the AuNP is surface-functionalized with OAm, it is expected that the AuNP reside within the OAm minority phase of a phase separated OAm/PMMA mixture. To this effect, there are three possibilities for why the well-dispersed nanoparticle states are seen in **Figure 3** and confirmed by SAXS (**Figure 4**): 1) reduced  $N_{PMMA}$  after the polymerization, which would favor miscibility, 2) AuNPs are in a metastable or kinetically trapped dispersion state that would otherwise phase separate given sufficient mobility, or 3) the OAm fraction in the phase separated domains is large enough to solubilize AuNPs and prevent aggregation.

Although the reported sample preparation method is different from conventional nanoparticle/polymer material preparation procedures, it is interesting to point out the resemblance between the OAm-functionalized AuNPs and polymer-functionalized nanoparticles. The coreshell structure of the OAm-functionalized AuNPs is effectively similar to a polymer-functionalized nanoparticle with a surface brush of small graft length ( $N_{OAm}$ ) and high graft density ( $\sigma$ ,  $\approx$  constant). Approximation of these structural parameters ( $N_{OAm} = 4$ ,  $\sigma \approx 1.2$  nm<sup>-2</sup>) gives a polymer-functionalized nanoparticle structure that would be predicted to adopt a phase separated or connected nanosheet preferred state in a polymer matrix with large matrix length ( $\sigma$  < 0.2). As a result, the trending toward aggregation from well-dispersed particles reported here matches our understanding of preferred polymer-functionalized nanoparticle/polymer material phases.  $\sigma$ 

## **CONCLUSIONS**

Here, we report a novel synthetic preparation method, termed RIPT, for creating AuNP/PMMA materials with sterically stable and variable nanoparticle dispersions. AuNPs were initially synthesized within an OAm/MMA mixture at room temperature, and were subsequently diluted to desired MMA volume fractions and thermally initiated to polymerize MMA. After the reaction, samples were evacuated of unreacted monomer and vacuum pressed to yield processed bulk materials. TEM and SAXS of processed samples exhibited hybrid materials with varied states of AuNP dispersion dependent on the reaction temperature and MMA volume fraction. The hybrid blends were found to maintain solution like AuNP dispersion throughout the reaction-induced phase transition from a solution to vitrified melt state and were observed to aggregate upon decreasing the MMA volume fraction during the drying stage. It is hypothesized that the OAm and PMMA components within these blends undergo phase separation as predicted by Flory-Huggins mixing theory, which effectively directs the OAm-functionalzed AuNPs into the minority OAm phase. As MMA is expected to be co-miscible within the OAm and PMMA phases, the removal of MMA from the OAm phase is hypothesized to drive AuNP aggregation. Despite the complex phase behavior observed, the reported process demonstrates resilience to thermal processing and annealing that preserves particle dimension and stability. Future work will investigate how processing techniques can be implemented to tune nanoparticle dispersion within this reactioninduced phase transition method to achieve intermediate states that lie between solution like dispersion and preferred equilibrium aggregate states.

## ASSOCIATED CONTENT

## **Supporting Information Available:**

The conversion of AuNP/PMMA blends; micrographs and UV-Vis spectra of AuNP/PMMA hybrid materials; nanoparticle size and interparticle spacing determined via image analysis and

SAXS analysis; experimentally determined viscosity values; summary of molecular weight and

 $N_{\rm PMMA}$  characteristics determined using SEC-MALS; viscometry measurements and discussion

are available in the Supporting Information. The Supporting Information is available free of charge

via the Internet at http://pubs.acs.org.

**AUTHOR INFORMATION** 

**Corresponding Author** 

\*E-mail: rjh64@psu.edu

**ORCID** 

Robert J. Hickey: 0000-0001-6808-7411

Robert A. Riggleman: 0000-0002-5434-4787

Jacob A. LaNasa: 0000-0003-3656-6682

**Author Contributions** 

J.L. performed the synthesis and sample processing. J.L. performed X-ray scattering, microscopy,

rheology, and thermal analysis measurements. A.N. and R.A.R. calculated the binodal curve. J.L.

and R.J.H. performed analysis and wrote the manuscript. All authors have given approval to the

final version of the manuscript.

Notes

The authors declare no competing financial interest.

**ACKNOWLEDGMENTS** 

This work was supported by the National Science Foundation (NSF), Division of Materials

Research Polymers Program (CAREER Proposal No.: DMR-1942508). All SAXS and TEM

measurements were taken at the Materials Characterization Lab (MCL) in the Materials Research

24

Institute (MRI) at the Pennsylvania State University. The authors are grateful to Yifan Xu for her help with UV-Vis, to Aijie Han for her assistance with viscometry, and to Missy Hazen for her service with microtoming polymer samples for TEM.

## **REFERENCES**

- (1) Kojima, Y.; Usuki, A.; Kawasumi, M.; Okada, A.; Fukushima, Y.; Kurauchi, T.; Kamigaito, O. Mechanical Properties of Nylon 6-Clay Hybrid. *J. Mater. Res.* **1993**, *8* (5), 1185–1189.
- (2) Kim, P.; Doss, N. M.; Tillotson, J. P.; Hotchkiss, P. J.; Pan, M. J.; Marder, S. R.; Li, J.; Calame, J. P.; Perry, J. W. High Energy Density Nanocomposites Based on Surface-Modified BaTiO 3 and a Ferroelectric Polymer. *ACS Nano* **2009**, *3* (9), 2581–2592.
- (3) Li, Q.; Chen, L.; Gadinski, M. R.; Zhang, S.; Zhang, G.; Li, H.; Haque, A.; Chen, L. Q.; Jackson, T.; Wang, Q. Flexible Higherature Dielectric Materials from Polymer Nanocomposites. *Nature* **2015**, *523* (7562), 576–579.
- (4) Kumar, S. K.; Benicewicz, B. C.; Vaia, R. A.; Winey, K. I. 50th Anniversary Perspective: Are Polymer Nanocomposites Practical for Applications? *Macromolecules* **2017**, *50* (3), 714–731.
- (5) Tchoul, M. N.; Fillery, S. P.; Koerner, H.; Drummy, L. F.; Oyerokun, F. T.; Mirau, P. A.; Durstock, M. F.; Vaia, R. A. Assemblies of Titanium Dioxide-Polystyrene Hybrid Nanoparticles for Dielectric Applications. *Chem. Mater.* 2010, 22 (5), 1749–1759.
- (6) Li, Y.; Tao, P.; Viswanath, A.; Benicewicz, B. C.; Schadler, L. S. Bimodal Surface Ligand Engineering: The Key to Tunable Nanocomposites. *Langmuir* **2013**, *29* (4), 1211–1220.
- (7) Hickey, R. J.; Koski, J.; Meng, X.; Riggleman, R. A.; Zhang, P.; Park, S. J. Size-Controlled Self-Assembly of Superparamagnetic Polymersomes. *ACS Nano* **2014**, *8* (1), 495–502.
- (8) Bockstaller, M. R.; Mickiewicz, R. A.; Thomas, E. L. Block Copolymer Nanocomposites: Perspectives for Tailored Functional Materials. *Adv. Mater.* **2005**, 17 (11), 1331–1349.

- (9) Lang, C.; LaNasa, J. A.; Utomo, N.; Xu, Y.; Nelson, M. J.; Song, W.; Hickner, M. A.; Colby, R. H.; Kumar, M.; Hickey, R. J. Solvent-Non-Solvent Rapid-Injection for Preparing Nanostructured Materials from Micelles to Hydrogels. *Nat. Commun.* 2019, 10 (1), 3855.
- (10) Howell, I. R.; Li, C.; Colella, N. S.; Ito, K.; Watkins, J. J. Strain-Tunable One Dimensional Photonic Crystals Based on Zirconium Dioxide/Slide-Ring Elastomer Nanocomposites for Mechanochromic Sensing. ACS Appl. Mater. Interfaces 2015, 7 (6), 3641–3646.
- (11) Qian, G.; Lin, Y.; Wantz, G.; Davis, A. R.; Carter, K. R.; Watkins, J. J. Saturated and Multi-Colored Electroluminescence from Quantum Dots Based Light Emitting Electrochemical Cells. *Adv. Funct. Mater.* 2014, 24 (28), 4484–4490.
- (12) Park, M.; Im, J.; Shin, M.; Min, Y.; Park, J.; Cho, H.; Park, S.; Shim, M. B.; Jeon, S.; Chung, D. Y.; Bae, J.; Park, J.; Jeong, U.; Kim, K. Highly Stretchable Electric Circuits from a Composite Material of Silver Nanoparticles and Elastomeric Fibres. *Nat. Nanotechnol.* **2012**, *7* (12), 803–809.
- (13) Gu, M.; Song, W.-J.; Hong, J.; Kim, S. Y.; Shin, T. J.; Kotov, N. A.; Park, S.; Kim, B.-S. Stretchable Batteries with Gradient Multilayer Conductors. *Sci. Adv.* **2019**, *5* (7), eaaw1879.
- (14) Hickey, R. J.; Haynes, A. S.; Kikkawa, J. M.; Park, S. J. Controlling the Self-Assembly Structure of Magnetic Nanoparticles and Amphiphilic Block-Copolymers: From Micelles to Vesicles. *J. Am. Chem. Soc.* **2011**, *133* (5), 1517–1525.
- (15) Hickey, R. J.; Meng, X.; Zhang, P.; Park, S. J. Low-Dimensional Nanoparticle Clustering in Polymer Micelles and Their Transverse Relaxivity Rates. *ACS Nano* **2013**, *7* (7), 5824—

5833.

- (16) Kumar, S. K.; Jouault, N.; Benicewicz, B.; Neely, T. Nanocomposites with Polymer Grafted Nanoparticles. *Macromolecules* **2013**, *46* (9), 3199–3214.
- (17) Hickey, R. J.; Seo, M.; Luo, Q.; Park, S. J. Directional Self-Assembly of Ligand-Stabilized Gold Nanoparticles into Hollow Vesicles through Dynamic Ligand Rearrangement. *Langmuir* **2015**, *31* (14), 4299–4304.
- (18) Ning, X.; Jimenez, A. M.; Pribyl, J.; Li, S.; Benicewicz, B.; Kumar, S. K.; Schadler, L. S. Nanoparticle Organization by Growing Polyethylene Crystal Fronts. ACS Macro Lett. 2019, 8 (10), 1341–1346.
- (19) Lanasa, J. A.; Hickey, R. J. Surface-Initiated Ring-Opening Metathesis Polymerization: A Method for Synthesizing Polymer-Functionalized Nanoparticles Exhibiting Semicrystalline Properties and Diverse Macromolecular Architectures. *Macromolecules* 2020, 53 (19), 8216–8232.
- (20) Nie, Z.; Fava, D.; Kumacheva, E.; Zou, S.; Walker, G. C.; Rubinstein, M. Self-Assembly of Metal-Polymer Analogues of Amphiphilic Triblock Copolymers. *Nat. Mater.* **2007**, *6* (8), 609–614.
- (21) Akcora, P.; Liu, H.; Kumar, S. K.; Moll, J.; Li, Y.; Benicewicz, B. C.; Schadler, L. S.; Acehan, D.; Panagiotopoulos, A. Z.; Pryamitsyn, V.; Ganesan, V.; Ilavsky, J.; Thiyagarajan, P.; Colby, R. H.; Douglas, J. F. Anisotropic Self-Assembly of Spherical Polymer-Grafted Nanoparticles. *Nat. Mater.* 2009, 8 (4), 354–359.
- Maguire, S. M.; Krook, N. M.; Kulshreshtha, A.; Bilchak, C. R.; Brosnan, R.; Pana, A.
   M.; Rannou, P.; Maréchal, M.; Ohno, K.; Jayaraman, A.; Composto, R. J. Interfacial
   Compatibilization in Ternary Polymer Nanocomposites: Comparing Theory and

- Experiments. *Macromolecules* **2021**, *54* (2), 797–811.
- (23) Sunday, D.; Ilavsky, J.; Green, D. L. A Phase Diagram for Polymer-Grafted Nanoparticles in Homopolymer Matrices. *Macromolecules* **2012**, *45* (9), 4007–4011.
- (24) Lü, C.; Gao, J.; Fu, Y.; Du, Y.; Shi, Y.; Su, Z. A Ligand Exchange Route to Highly Luminescent Surface-Functionalized ZnS Nanoparticles and Their Transparent Polymer Nanocomposites. *Adv. Funct. Mater.* **2008**, *18* (19), 3070–3079.
- (25) Gallei, M. Functional Polymer Opals and Porous Materials by Shear-Induced Assembly of Tailor-Made Particles. *Macromol. Rapid Commun.* **2018**, *39* (4), 1700648.
- (26) Mandal, T.; Fleming, M.; Walt, D. R. Preparation of Polymer Coated Gold Nanoparticles by Surface-Confined Living Radical Polymerization at Ambient Temperature. *Nano Lett.* **2002**, *2* (1), 3–7.
- (27) Hore, M. J. A. Polymers on Nanoparticles: Structure & Dynamics. Soft Matter 2019, 15(6), 1120–1134.
- (28) Hui, C. M.; Pietrasik, J.; Schmitt, M.; Mahoney, C.; Choi, J.; Bockstaller, M. R.; Matyjaszewski, K. Surface-Initiated Polymerization as an Enabling Tool for Multifunctional (Nano-)Engineered Hybrid Materials. *Chem. Mater.* 2014, 26 (1), 745–762.
- (29) Bartholome, C.; Beyou, E.; Bourgeat-Lami, E.; Chaumont, P.; Lefebvre, F.; Zydowicz, N. Nitroxide-Mediated Polymerization of Styrene Initiated from the Surface of Silica Nanoparticles. In Situ Generation and Grafting of Alkoxyamine Initiators.

  Macromolecules 2005, 38 (4), 1099–1106.
- (30) Pyun, J.; Jia, S.; Kowalewski, T.; Patterson, G. D.; Matyjaszewski, K. Synthesis and Characterization of Organic/Inorganic Hybrid Nanoparticles: Kinetics of Surface-Initiated

- Atom Transfer Radical Polymerization and Morphology of Hybrid Nanoparticle Ultrathin Films. *Macromolecules* **2003**, *36* (14), 5094–5104.
- (31) Ohno, K.; Akashi, T.; Huang, Y.; Tsujii, Y. Surface-Initiated Living Radical Polymerization from Narrowly Size-Distributed Silica Nanoparticles of Diameters Less than 100 Nm. *Macromolecules* **2010**, *43* (21), 8805–8812.
- (32) Chandran, S.; Begam, N.; Padmanabhan, V.; Basu, J. K. Confinement Enhances

  Dispersion in Nanoparticle-Polymer Blend Films. *Nat. Commun.* **2014**, *5* (1), 1–9.
- (33) Hu, Y.; Zhou, S.; Wu, L. Surface Mechanical Properties of Transparent Poly(Methyl Methacrylate)/Zirconia Nanocomposites Prepared by in Situ Bulk Polymerization. *Polymer* **2009**, *50* (15), 3609–3616.
- (34) Li, L.; Miesch, C.; Sudeep, P. K.; Balazs, A. C.; Emrick, T.; Russell, T. P.; Hayward, R.
   C. Kinetically Trapped Co-Continuous Polymer Morphologies through Intraphase
   Gelation of Nanoparticles. *Nano Lett.* 2011, *11* (5), 1997–2003.
- (35) Chandran, S.; Baschnagel, J.; Cangialosi, D.; Fukao, K.; Glynos, E.; Janssen, L. M. C.; Müller, M.; Muthukumar, M.; Steiner, U.; Xu, J.; Napolitano, S.; Reiter, G. Processing Pathways Decide Polymer Properties at the Molecular Level. *Macromolecules* 2019, 52 (19), 7146–7156.
- (36) Zhao, D.; Gimenez-Pinto, V.; Jimenez, A. M.; Zhao, L.; Jestin, J.; Kumar, S. K.; Kuei, B.; Gomez, E. D.; Prasad, A. S.; Schadler, L. S.; Khani, M. M.; Benicewicz, B. C. Tunable Multiscale Nanoparticle Ordering by Polymer Crystallization. ACS Cent. Sci. 2017, 3 (7), 751–758.
- (37) Abetz, V.; Kremer, K.; Müller, M.; Reiter, G. Functional Macromolecular Systems: Kinetic Pathways to Obtain Tailored Structures. *Macromol. Chem. Phys.* **2019**, *220* (2),

- 1800334.
- (38) Grabowski, C. A.; Adhikary, B.; Mukhopadhyay, A. Dynamics of Gold Nanoparticles in a Polymer Melt. *Appl. Phys. Lett.* **2009**, *94* (2), 021903.
- (39) Grabowski, C. A.; Mukhopadhyay, A. Size Effect of Nanoparticle Diffusion in a Polymer Melt. *Macromolecules* **2014**, *47* (20), 7238–7242.
- (40) Carroll, B.; Bocharova, V.; Carrillo, J. M. Y.; Kisliuk, A.; Cheng, S.; Yamamoto, U.; Schweizer, K. S.; Sumpter, B. G.; Sokolov, A. P. Diffusion of Sticky Nanoparticles in a Polymer Melt: Crossover from Suppressed to Enhanced Transport. *Macromolecules* 2018, 51 (6), 2268–2275.
- (41) Cai, L. H.; Panyukov, S.; Rubinstein, M. Hopping Diffusion of Nanoparticles in Polymer Matrices. *Macromolecules* **2015**, *48* (3), 847–862.
- (42) Seo, M.; Hillmyer, M. A. Reticulated Nanoporous Polymers by Controlled Polymerization-Induced Microphase Separation. *Science* **2012**, *336* (6087), 1422–1425.
- (43) Lequieu, J.; Magenau, A. J. D. Reaction-Induced Phase Transitions with Block Copolymers in Solution and Bulk. *Polym. Chem.* **2021**, *12*, 12-28.
- (44) Kojima, Y.; Usuki, A.; Kawasumi, M.; Okada, A.; Kurauchi, T.; Kamigaito, O. Synthesis of Nylon 6–Clay Hybrid by Montmorillonite Intercalated with E-caprolactam. *J. Polym. Sci. Part A Polym. Chem.* 1993, 31 (4), 983–986.
- (45) Dean, L. M.; Ravindra, A.; Guo, A. X.; Yourdkhani, M.; Sottos, N. R. Photothermal Initiation of Frontal Polymerization Using Carbon Nanoparticles. ACS Appl. Polym. Mater. 2020, 2 (11), 4690–4696.
- (46) Schmarsow, R. N.; dell'Erba, I. E.; Villaola, M. S.; Hoppe, C. E.; Zucchi, I. A.; Schroeder, W. F. Effect of Light Intensity on the Aggregation Behavior of Primary

- Particles during in Situ Photochemical Synthesis of Gold/Polymer Nanocomposites. *Langmuir* **2020**, *36* (46), 13759–13768.
- (47) Caruso, M. M.; Davis, D. A.; Shen, Q.; Odom, S. A.; Sottos, N. R.; White, S. R.; Moore, J. S. Mechanically-Induced Chemical Changes in Polymeric Materials. *Chem. Rev.* 2009, 109 (11), 5755–5798.
- (48) Lloyd, E. M.; Feinberg, E. C.; Gao, Y.; Peterson, S. R.; Soman, B.; Hemmer, J.; Dean, L. M.; Wu, Q.; Geubelle, P. H.; Sottos, N. R.; Moore, J. S. Spontaneous Patterning during Frontal Polymerization. ACS Cent. Sci. 2021, 7 (4), 603–612.
- (49) Lanasa, J. A.; Torres, V. M.; Hickey, R. J. In Situ Polymerization and Polymer Grafting to Stabilize Polymer-Functionalized Nanoparticles in Polymer Matrices. *J. Appl. Phys.* **2020**, *127* (13), 134701.
- (50) Hou, D.; Bostwick, J. E.; Shallenberger, J. R.; Zofchak, E. S.; Colby, R. H.; Liu, Q.; Hickey, R. J. Simultaneous Reduction and Polymerization of Graphene Oxide/Styrene Mixtures to Create Polymer Nanocomposites with Tunable Dielectric Constants. ACS Appl.Nano Mater. 2020, 3 (2), 962-968.
- (51) Peng, S.; Lee, Y.; Wang, C.; Yin, H.; Dai, S.; Sun, S. A Facile Synthesis of Monodisperse Au Nanoparticles and Their Catalysis of CO Oxidation. *Nano Res.* **2008**, *1* (3), 229–234.
- (52) Hiemenz, P. C.; Lodge, T. P. Polymer Chemistry, 2nd ed.; 2007.
- (53) Storhoff, J. J.; Lazarides, A. A.; Mucic, R. C.; Mirkin, C. A.; Letsinger, R. L.; Schatz, G.
  C. What Controls the Optical Properties of DNA-Linked Gold Nanoparticle Assemblies?
  J. Am. Chem. Soc. 2000, 122 (19), 4640–4650.
- (54) Balke, S. T.; Hamielec, A. E. Bulk Polymerization of Methyl Methacrylate. *J. Appl. Polym. Sci.* **1973**, *17* (3), 905–949.

- (55) Di Mauro, A. E.; Striccoli, M.; Depalo, N.; Fanizza, E.; Cano, L.; Ingrosso, C.; Agostiano, A.; Curri, M. L.; Tercjak, A. Selective Confinement of Oleylamine Capped Au Nanoparticles in Self-Assembled PS-b-PEO Diblock Copolymer Templates. *Soft Matter* 2014, 10 (11), 1676–1684.
- (56) Zofchak, E. S.; Lanasa, J. A.; Torres, V. M.; Hickey, R. J. Deciphering the Complex Phase Behavior during Polymerization-Induced Nanostructural Transitions of a Block Polymer/Monomer Blend. *Macromolecules* **2020**, *53* (3), 835–843.